International Journal of Minerals, Metallurgy and Materials
Volume 25, Number 2, February 2018, Page 190
https://doi.org/10.1007/s12613-018-1562-2

Formation of microstructural features in hot-dip aluminized AISI 321 stainless steel

Prashant Huilgol, K. Rajendra Udupa, and K. Udaya Bhat

Department of Metallurgical & Materials Engineering, National Institute of Technology Karnataka, Surathkal, Mangalore-575025, India
(Received: 17 May 2017; revised: 26 October 2017; accepted: 27 October 2017)

Abstract: Hot-dip aluminizing (HDA) is a proven surface coating technique for improving the oxidation and corrosion resistance of ferrous substrates. Although extensive studies on the HDA of plain carbon steels have been reported, studies on the HDA of stainless steels are limited. Because of the technological importance of stainless steels in high-temperature applications, studies of their microstructural development during HDA are needed. In the present investigation, the HDA of AISI 321 stainless steel was carried out in a pure Al bath. The microstructural features of the coating were studied using scanning electron microscopy and transmission electron microscopy. These studies revealed that the coating consists of two regions: an Al top coat and an aluminide layer at the interface between the steel and Al. The Al top coat was found to consist of intermetallic phases such as Al_7Cr and Al_3Fe dispersed in an Al matrix. Twinning was observed in both the Al_7Cr and the Al_3Fe phases. Furthermore, the aluminide layer comprised a mixture of nanocrystalline Fe_2Al_5, Al_7Cr, and Al. Details of the microstructural features are presented, and their formation mechanisms are discussed.

Keywords: hot-dip aluminizing; aluminide layer; intermetallic phases; microstructural features; stainless steel

1. Introduction

Stainless steels are used widely along with titanium-based alloys, aluminides, and superalloys in a vast number of high-temperature applications. Stainless steel of grade AISI 321 is used in aerospace exhaust manifolds, components for the nuclear industry, jet engine parts, and chemical processing equipment. It is also used as a structural material in fusion reactors. Recently, grade AISI 321 aluminized stainless steels have been reported to be effective deuterium and tritium permeation barriers [1–2]. They offer the benefits of reasonable high-temperature strength, adequate creep resistance and good oxidation and corrosion resistance. However, at elevated temperatures (e.g., > 700°C) and in aggressive environments, protection is needed against degradation phenomena such as cyclic oxidation, high-temperature corrosion, and solid-particle abrasion. Aluminizing of steel is expected to overcome such problems because Al forms a compact layer of Al_2O_3, which provides improved resistance to oxidation and corrosion at elevated temperatures and in severe corrosive environments.

The aluminizing of steel can be carried out via different routes, the details of which have been reviewed by Bhat [3]. Hot-dip aluminizing (HDA) of carbon steel has been studied extensively, especially from the viewpoint of microstructure formation [4–8]. The major intermetallic phases identified during HDA of low-carbon steel are Fe_2Al_5 and $FeAl_3$. These Al-rich phases are brittle in nature, and the coating may crack and peel off during secondary operations such as bending and machining. A secondary diffusion treatment is necessary to transform these phases into comparatively ductile Fe-rich phases such as FeAl and Fe_3Al [9].

The HDA of alloy steels has been less extensively studied than that of carbon steels. Wang and Shi [5] reported the formation of Fe_2Al_5 and $Al_{13}Cr_2$ phases during HDA of 1Cr18Ni9 stainless steels in a pure Al bath. Dybkov [10] reported the formation of Fe_2Al_7 and Al_7Cr phases during HDA of Fe–Cr steel using a pure Al bath at 700°C. The phases were discontinuous and scattered in the Al top coat, and Fe_2Al_5 was observed as a continuous phase. In both of

Corresponding author: Prashant Huilgol E-mail: prashanthuilgol@gmail.com

the aforementioned investigations, the phase analysis was carried out using X-ray diffraction and scanning electron microscopy (SEM). Very little information was reported about the presence of fine second-phase precipitates or the growth of thin intermetallic layers. To the best of our knowledge, the literature contains no investigations of the microstructures formed during HDA of AISI 321. In this investigation, the formation of microstructural features during HDA of AISI 321 using a bath of commercial pure Al is discussed.

2. Experimental

The AISI 321 stainless steel base material with a composition Cr 17.8%, Ni 11.5%, C 0.07%, Mn 1.58%, Si 0.04%, Ti 0.64%, S 0.006%, P 0.012%, and Fe bal. (all in wt%) was used in this investigation. Commercial pure Al was melted in a clay graphite crucible in a temperature-controlled electric resistance furnace. The temperature of the molten Al was maintained at (700 ± 1)°C. The bath was covered with commercially available coverall flux. Coupons in plate form with dimensions of 40 mm × 10 mm × 3 mm were polished and degreased. One end of the coupon was tied with nichrome wire and immersed in a molten bath for 10 min. The coupons were then removed and cooled in air. After the aluminizing process, the samples were cut across their cross section and metallographically polished. Their microstructures were characterized using a scanning electron microscope (SEM, JEOL, model6380LA) equipped with an energy-dispersive spectrometer (EDS), a field-emission scanning electron microscope (Carl Ziess AG, modelSupra 40-FESEM), and a transmission electron microscope (TEM, JEM-2100) also equipped with an energy-dispersive spectrometer. For study of fine particles by transmission electron microscopy–energy-dispersive spectroscopy (TEM–EDS), an electron beam size in the range of 1–25 nm was used. The beam size was varied depending on the particle size.

A series of samples were prepared for TEM studies starting from the Al side toward the base-metal side. The samples were thinned, punched into 3-mm discs, dimpled, and then ion milled using a GATAN (PIPS) ion-milling machine until the samples were electron transparent.

The coating thickness was measured for three coupons and at three different locations within each coupon. The average value is reported.

3. Results

Fig. 1(a) presents a cross-sectional backscattered electron (BSE) SEM micrograph showing an Al coating on the surface of AISI 321 steel. The coating appears to be uniform in thickness throughout. The average coating thickness is in the range of (43 ± 0.3) μm. Fig. 1(b) presents a magnified micrograph of the region shown in Fig. 1(a). It shows three distinct regions: region 1, region 2, and the base metal. Region 1 is the aluminide layer formed at the interface between steel and Al; it is (12 ± 3) μm thick. Region 2 is an Al top coat with intermetallic phases distributed in the Al matrix with a thickness of approximately (32 ± 2.5) μm. The detailed analyses of the microstructural features are presented and discussed in subsequent sections.

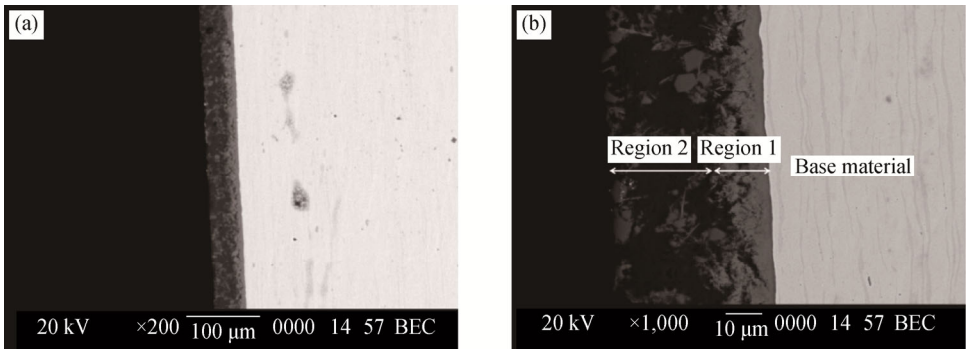

Fig. 1. Low-magnification SEM-BSE micrograph of an aluminized sample showing a coating of uniform thickness (a) and magnified view of a selected region from subfigure (a), showing three distinct regions (b).

3.1. Region 1: the aluminide layer

An intermediate aluminide layer was formed at the interface between the base material and Al, as shown in Fig. 1(b). The SEM-BSE micrograph in Fig. 2 shows varying contrast within the aluminide layer, revealing that the layer consists of a mixture of phases. These features were further analyzed by TEM.

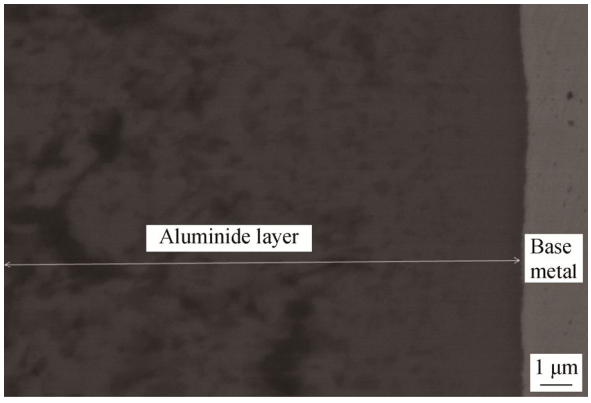

Fig. 2. SEM-BSE micrograph showing a mixture of phases in the aluminide layer (region 1).

The TEM images reveal fine grains of Fe_2Al_5 and Al_7Cr along with Al in this layer (Figs. 3 and 4). Fig. 3(a) shows clusters of the Fe_2Al_5 phase along with Al. These clusters are essentially submicron size. Nanocrystalline grains with an average grain size of approximately 40 nm are observed within these clusters. These grains are evident in the higher-magnification micrograph shown in Fig. 3(b). The selected-area electron diffraction (SAED) pattern is shown as the inset in Fig. 3(b). The composition obtained via TEM–EDS is 70.4at% Al, 26.7at% Fe, 1.7at% Cr, and 1.2at% Ni, which is consistent with the composition of the Fe_2Al_5 phase. This phase dissolves as much as 2at% Ni at 1050°C [11] and as much as 6.2at% Cr at 1000°C [12].

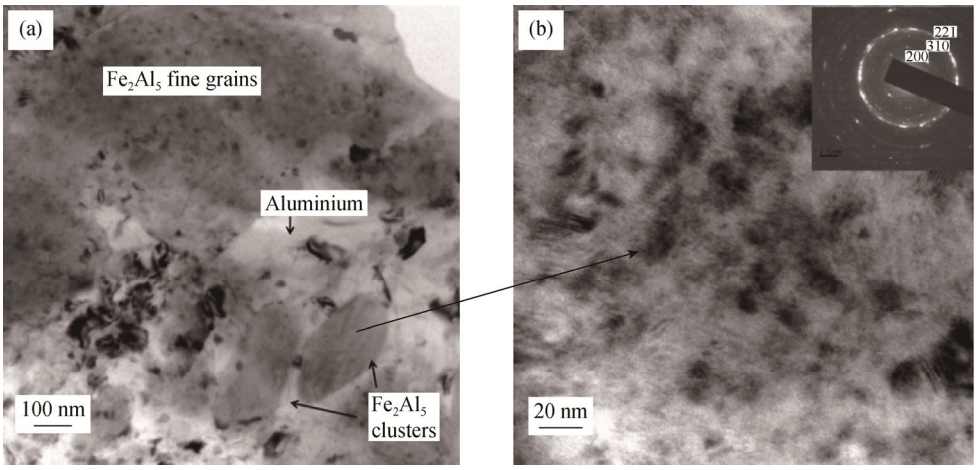

Fig. 3. Bright-field TEM micrograph showing clusters of the Fe_2Al_5 phase (a) and fine grains of Fe_2Al_5 (the SAED pattern is shown in the inset) (b).

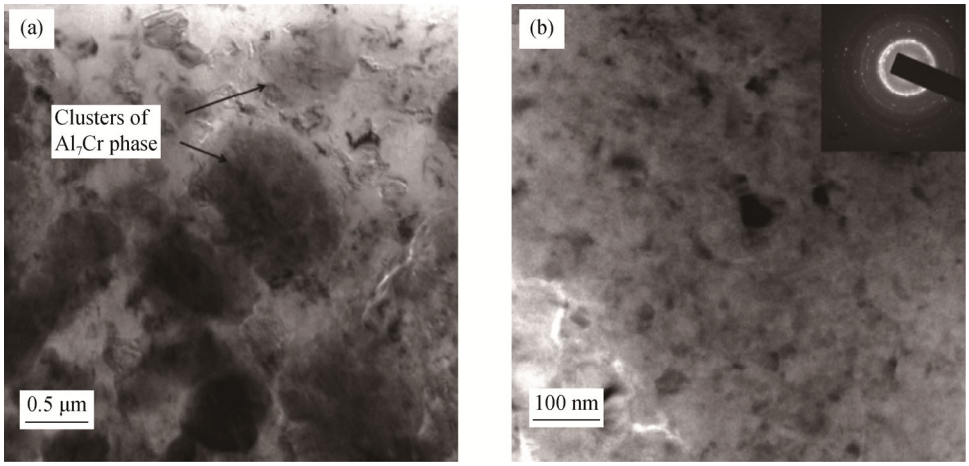

Fig. 4 Bright-field TEM micrograph showing clusters of the Al_7Cr phase (a) and high-magnification micrograph showing the fine-grain structure of Al_7Cr observed within the cluster (the inset shows the corresponding SAED pattern) (b).

Fig. 4(a) shows a TEM micrograph of clusters of the Al_7Cr phase. Similar to the Fe_2Al_5 phase, a fine-grain microstructure is observed. This microstructure is shown at high magnification (Fig. 4(b)). TEM–EDS elemental analysis of this phase shows that the composition is 81at% Al, 13.9at% Cr, 4.1at% Fe, and 1at% Ni. This composition is in close agreement with that reported in the literature. The Al_7Cr phase shows increased iron solubility of 4.1at%,

whereas the reported value is 2.2at% [12]. Region 1, i.e., the aluminide layer, consists of Fe_2Al_5, Al_7Cr, and Al. Fine-grain-sized Al is observed surrounding the clusters of Fe_2Al_5 and Al_7Cr phases. Fig. 5(a) shows the fine grains of Al; the associated polycrystalline diffraction pattern is shown in Fig. 5(b).

3.2. Region 2: Al top coat

Region 2 has a continuous gray Al matrix, in contrast with the bright Al-based intermetallic phases. The details of these features are revealed in the photomicrograph presented in Fig. 6. Two categories of morphologies are identified for intermetallic phases: acicular and polygonal. They are denoted as A and C, respectively. SEM–EDS analysis indicates that morphology A corresponds to an Al–Fe intermetallic phase with a composition similar to that of Al_3Fe and that morphology C corresponds to the Al–Cr intermetallic phase with a composition similar to that of Al_7Cr. This fact was also subsequently confirmed by TEM studies. These phases are distributed throughout the top coat embedded in the Al matrix. The size of the Al_7Cr phase ranges from the sub-micrometer scale to approximately 5 μm. The Al_3Fe phase is acicular shaped, with a length of 2 to 3 μm and a width of approximately 0.5 μm or less.

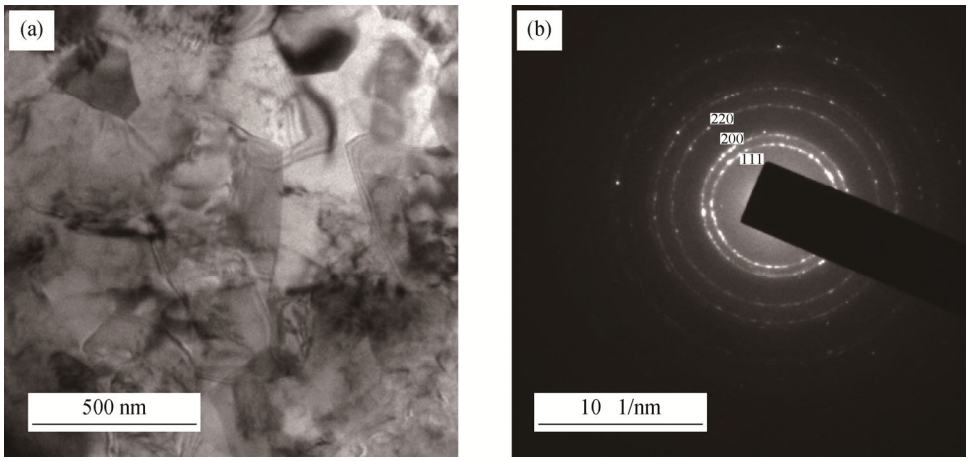

Fig. 5. Bright-field TEM micrograph showing nanocrystalline Al grains (a) and the associated diffraction pattern (b).

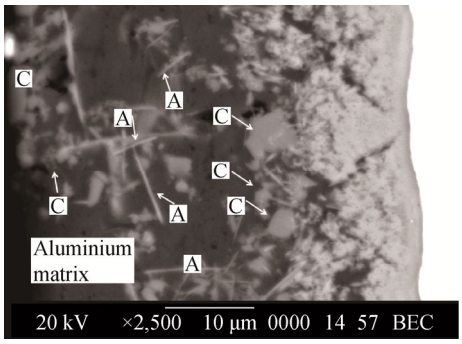

Fig. 6. SEM micrograph of region 2 in the Al top coat, showing a polygonal-shaped Al_7Cr phase and acicular-shaped Al_3Fe phase embedded in the Al matrix.

3.2.1. The Al_7Cr phase

Fig. 7(a) is a bright-field TEM micrograph showing a polygonal Al_7Cr phase distributed in the Al matrix. The TEM–EDS analysis results, as presented in Fig. 7(b), indicate that the composition is 84.9at% Al, 12.3at% Cr, and 2.8at% Fe, which is similar to that of the Al_7Cr phase. The crystal structure of the Al_7Cr phase has been reported to be of C-centered monoclinic type with space group *C*2/*m* [13–14]. Within the Al_7Cr phase, spherical precipitates of 60–70 nm in size are observed. TEM–EDS analysis shows that the composition of the spherical precipitates is 53.6at% Al, 40.8at% Fe, and 5.6at% Cr. Furthermore, the same analysis indicates that the solubility of Cr in the Al matrix is almost nil. Twinning around the (001) plane is observed in the Al_7Cr phase. Figs. 8(a) and 8(b) show a TEM micrograph of twinned Al_7Cr and its associated SAED pattern, respectively.

3.2.2. The Al_3Fe phase

In the Al top coat, plates of Al_3Fe are observed along with the Al_7Cr phase. Fig. 9(a) shows a bright-field TEM micrograph of Al_3Fe plates present in the Al top coat, and Fig. 9(b) shows the TEM–EDS spectrum corresponding to the Al_3Fe phase. The TEM–EDS analysis results indicate that the composition is 75.8at% Al, 20.3at% Fe, 1.4at% Cr, and 2.5at% Ni. Most of the plates are in the range from 1 to 3 μm in length. At higher magnifications, twins within these plates are also discernible. Fig. 10(a) presents higher-magnification bright-field TEM micrograph that show twinning within the Al_3Fe plates. Fig. 10(b) shows the dif-

fraction pattern of the twinned Al_3Fe phase.

3.2.3. Al matrix

Fig. 11 shows the microstructural features observed in region 2 of the Al matrix. The average grain size of the Al matrix measures approximately 1–2 μm. A large number of dislocations are observed in the Al grains (Fig. 11). Elements such as Fe, Cr, and Ni were not detected in this region by TEM–EDS analysis. Notably, binary phase diagrams of Al–Fe, Al–Cr, and Al–Ni show negligible solubility of solutes (Fe, Ni, or Cr) in Al at room temperature [15].

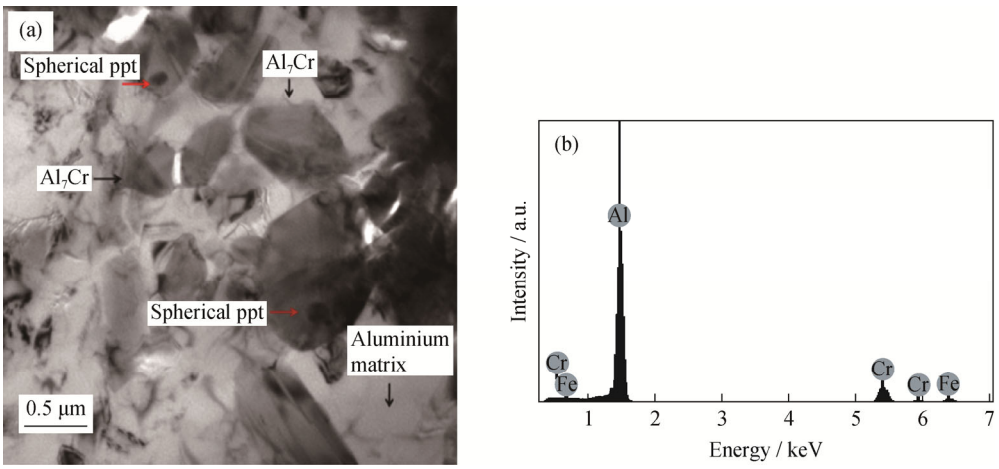

Fig. 7. Bright-field TEM micrograph showing the Al_7Cr phase in an Al matrix (a) and TEM–EDS spectrum of the Al_7Cr phase (b).

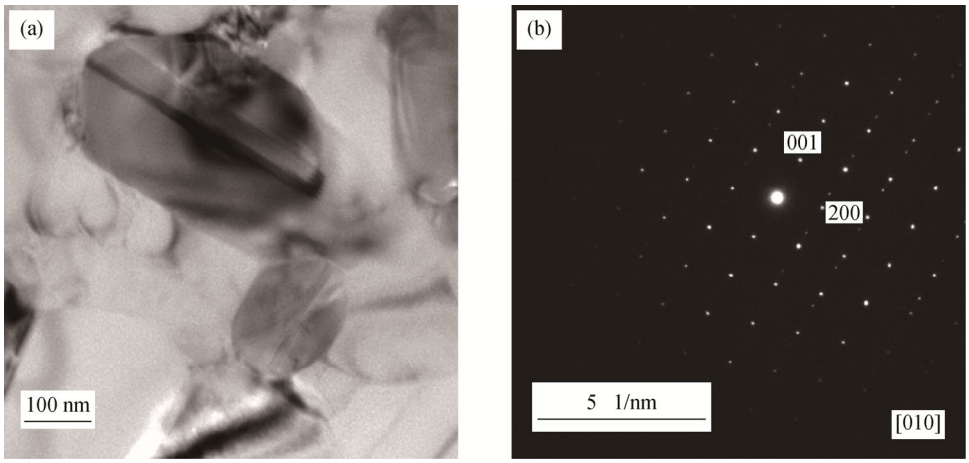

Fig. 8. Bright-field TEM micrograph showing a twinned Al_7Cr phase (a) and diffraction pattern showing twinning around the (001) plane (b).

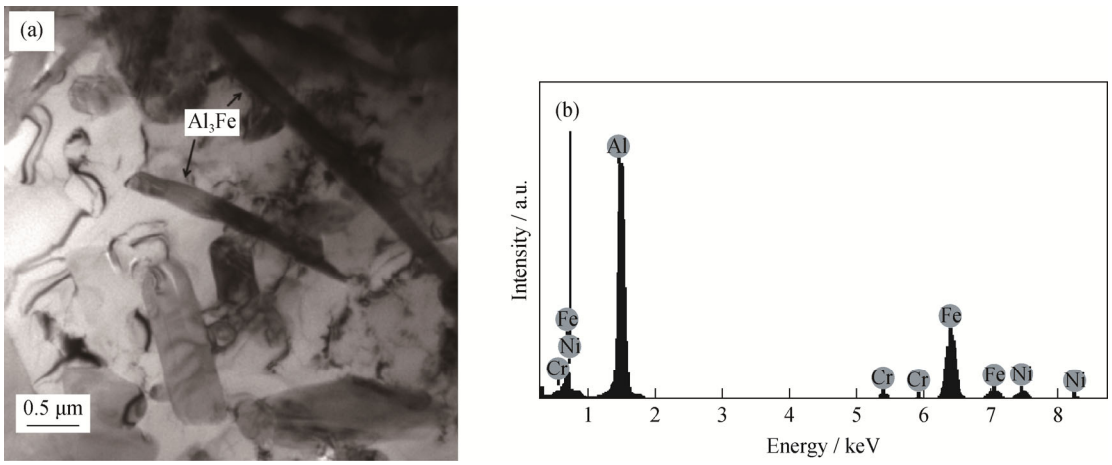

Fig. 9. Bright-field TEM micrograph showing Al_3Fe plates formed in the Al top coat (a) and TEM–EDS spectrum of the Al_3Fe phase (b).

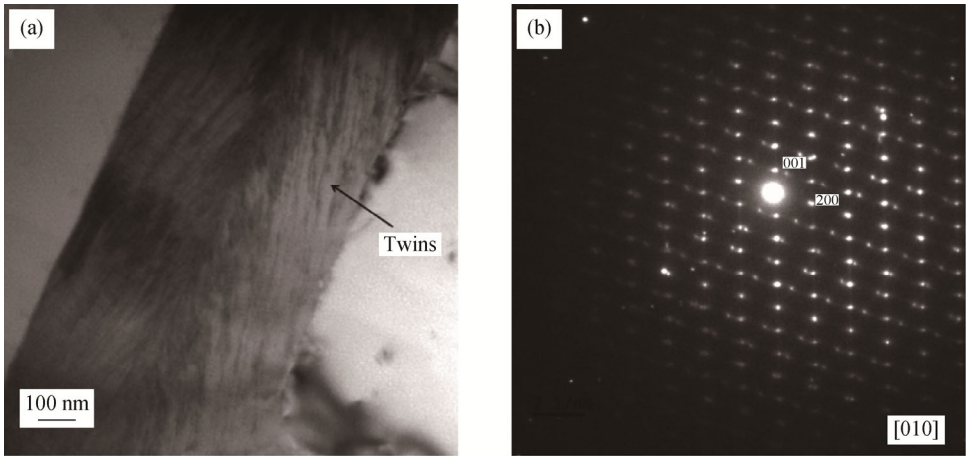

Fig. 10. Bright-field TEM micrograph showing twins in the Al_3Fe phase (a) and diffraction pattern of twinned Al_3Fe (b).

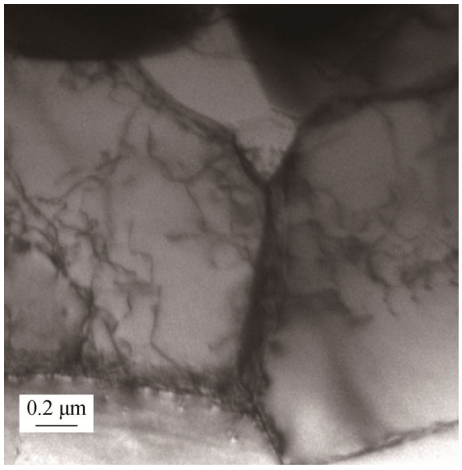

Fig. 11. Bright-field TEM micrograph showing a large amount of dislocations in Al grains in region 2.

3.3. Base material

The base material region very near the interface exhibits a fine-grained microstructure, as shown in Fig. 12(a). The average grain size is in the range of 30–40 nm. The SAED pattern (inset of Fig. 12(a)) reveals the structure as ferritic (body-centered cubic), in contrast to the austenitic (face-centered cubic) phase of the base metal. This region is richer in Cr, with the composition of 31at% Cr, 63at% Fe, 3.69at% Ni, and 1.73at% Si. The corresponding TEM–EDS spectrum is presented in Fig. 12(b).

The microstructure of the base metal away from the interface is austenitic. The microstructure is shown in Fig. 13(a), and the corresponding diffraction pattern of the austenite phase is shown in Fig. 13(b).

4. Discussion

4.1. Region 1: the aluminide layer

Fig. 14 shows the isothermal section of the ternary phase diagram of Al–Cr–Fe at 700°C. At the Al-rich corner, a three-phase equilibrium of "Al_7Cr + Al_3Fe + liquid" Al is established. The elemental Fe or Cr has limited solubility in

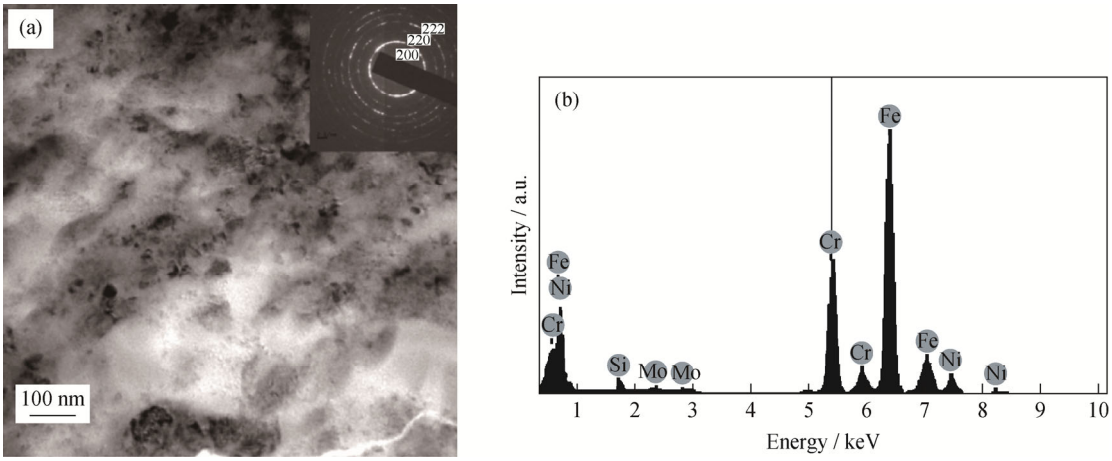

Fig. 12. Bright-field TEM micrograph of the base material adjacent to the interface (a) and TEM–EDS spectrum showing a higher Cr content (b).

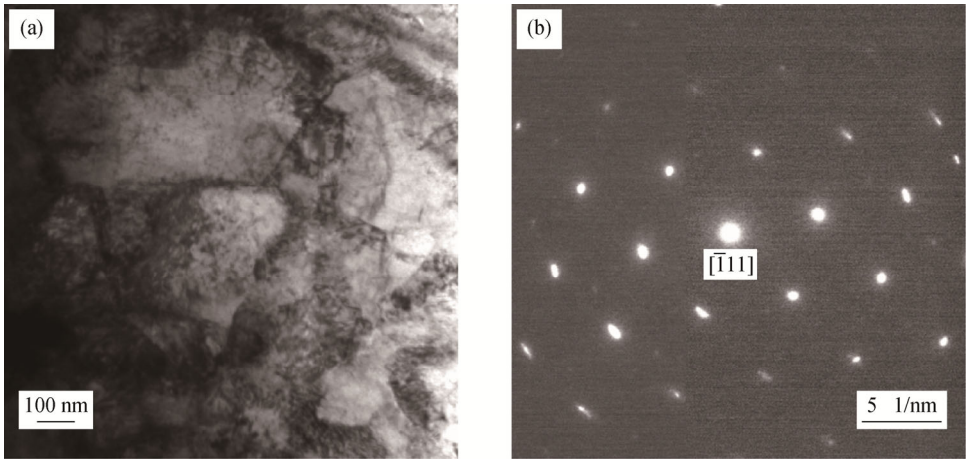

Fig. 13. Bright-field TEM micrograph of the base metal away from the interface (a) and the corresponding SAED pattern indicating a face-centered cubic structure (b).

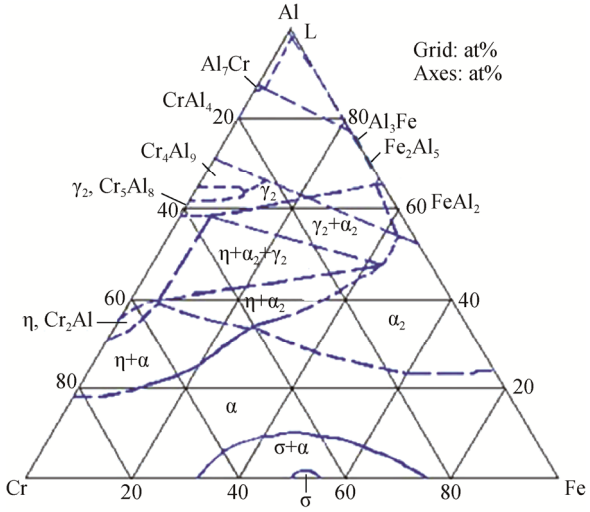

Fig. 14. Al–Cr–Fe isothermal section at 700°C [16].

liquid Al at 700°C. The intermetallic compound Al_7Cr is formed by the invariant reaction "liquid + $Al_{11}Cr_2 \leftrightarrow Al_7Cr$", whereas Al_3Fe is formed by eutectic reaction at 655°C.

In the present investigation, the base material was immersed into a molten Al bath maintained at 700°C. At the instant where the base metal contacted the molten Al, two events are expected to occur: (i) solidification of Al on the surface of the base metal because of rapid cooling and (ii) dissolution of elements from the base metal to establish equilibrium.

A part of the solidified Al layer remelts as the heat transfer continues. Dissolution or melting occurs because the composition at the interface is far from equilibrium. This melting is the result of solute transport across the interface rather than thermally driven melting. Such solutal melting has been reported to occur during welding of dissimilar metals [17]. Furthermore, because the dissolution process continues, a concentration profile develops at the interface. The concentration of any one of these elements at a particular distance from the interface is decided by two factors: (i) the enrichment rate of solute because of the dissolution process and (ii) the depletion rate of solute atoms from the interface because of the diffusion process.

A hypothetical concentration profile ahead of the stainless steel substrate is shown in Fig. 15. Parameter C_m is the metastable concentration, C_s is the equilibrium concentration, and C_∞ is the concentration far from the interface. Higher concentrations (higher than the equilibrium concentration) of elements are expected because the system is under nonequilibrium conditions. Because the liquid Al is supersaturated with elements, a strong driving force for nucleation of intermetallics exists. The process of nucleation of solid particles from the melt is a complex phenomenon because the energy barrier associated with the nucleation is required to be overcome by supersaturation of liquid with respect to Fe or Cr. The higher the supersaturation, the better the chance of survival of newly born nuclei. Therefore, it is likely that a greater number of fine nuclei form near the interface. The solidification temperature of the intermetallics is greater than 700°C, and they are expected to nucleate and attempt to grow. Nucleation of Al_3Fe and Al_7Cr phases are expected to occur in the liquid state according to the ternary equilibrium diagram. However, in our study, Fe_2Al_5 and Al_7Cr phases are observed. The heat of formation for the Fe_2Al_5 phase is more negative than that for the Al_3Fe phase [18], which indicates that the interatomic bonds in Fe_2Al_5 are stronger than those in Al_3Fe. Also, the composition obtained from TEM–EDS analysis is similar to that of the Fe_2Al_5 phase. Notably, not only thermodynamic aspects but also kinetics plays a vital role in the nucleation and growth

of intermetallics phases. Kinetically, the Fe_2Al_5 phase is more strongly favored because of its open structure. Several models have been put forth by researchers to predict first phase nucleation and subsequent phase formation [19–21]. The phase with the highest growth rate is expected to form. In addition, Fe_2Al_5 has been observed to exhibit the highest growth rate among various intermetallic phases in the Al–Fe system [22].

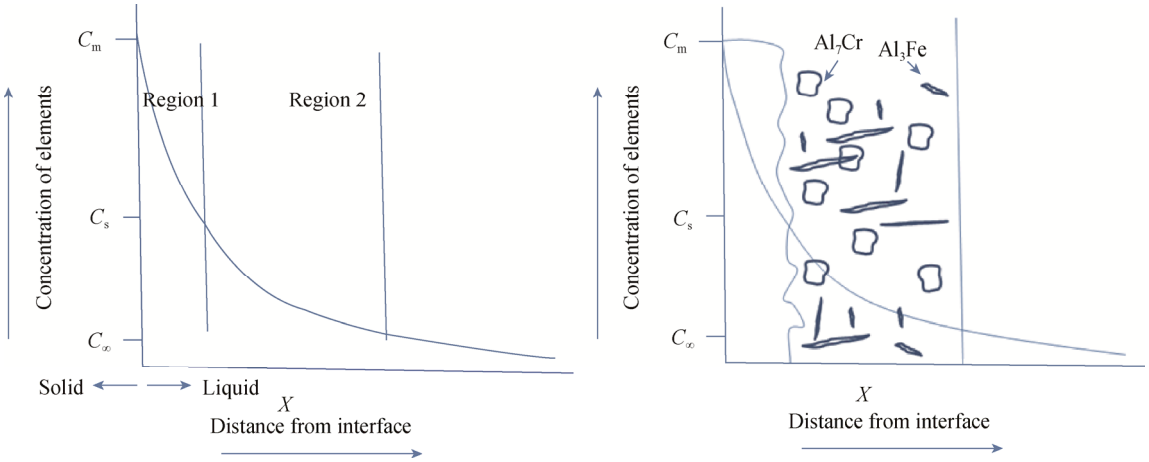

Fig. 15. Schematic representation of a hypothetical concentration profile of elements ahead of the solid–liquid interface.

4.2. Region 2: the Al top coat

The formation of an aluminide layer at the interface affects the shape of the concentration profile ahead of the aluminide layer. The nucleation of intermetallics reduces the supersaturation, and dissolution thereby continues. The dissolved elements that do not participate in the nucleation of intermetallics diffuse away from the interface. The concentration of elements decreases as moving away from the interface. Equilibrium phases Al_7Cr and Al_3Fe phases nucleate and grow in the liquid state if the concentration is greater than the equilibrium concentration or form by precipitation during cooling to room temperature. At a temperature of approximately 655°C and a composition very close to that of pure Al, an invariant point exists to form Al/Al_3Fe eutectic. According to the Al–Cr equilibrium phase diagram, at 661.4°C, an Al solid solution forms by peritectic reaction [23]. Therefore, Al_7Cr can nucleate and grow in the liquid state, whereas Al_3Fe can form in the melt or precipitate via eutectic reaction during cooling.

4.3. Base metal

During interdiffusion of Al with the austenitic stainless steel, the austenite phase has been reported to transform to a ferritic phase [24]. Al diffusion into the steel increases the Cr equivalent (Cr_{eq}), thereby stabilizing the ferritic phase. The present study does not show any Al content determined by TEM–EDS analysis. Contrarily, the base metal dissolves when brought in contact with the molten Al. Nickel preferentially dissolves during this process because of its greater solubility in molten Al. The depletion of Ni leads to destabilization of austenite phase; hence, the ferritic phase is observed. Furthermore, the melted substrate region undergoes solidification, forming a fine-grained microstructure during cooling.

5. Conclusions

(1) AISI 321 stainless steel was hot-dip aluminized at 700°C for 10 min using a pure Al bath.

(2) The coating consists of two regions: an Al top coat and an intermediate nanocrystalline aluminide layer.

(3) The top coat consists of Al_7Cr and Al_3Fe intermetallic phases dispersed in the Al matrix and the aluminide layer comprises of nanocrystalline Fe_2Al_5, Al_7Cr, and Al.

(4) The formation of the aluminide layer is due to the nucleation of phases as a result of increased concentration at the interface because of dissolution of the base metal.

(5) In region 2, Al_7Cr nucleates and grows in the liquid state, whereas the Al_3Fe phase can form in the melt or precipitate via eutectic reaction during cooling.

Acknowledgements

One of the authors (P H) would like to thank MHRD, Government of India, for providing a research fellowship.

References

[1] F.L. Yang, X. Xiang, G.D. Lu, G.K. Zhang, T. Tang, Y. Shi,

and X.L. Wang, Tritium permeation characterization of Al_2O_3/FeAl coatings as tritium permeation barriers on 321 type stainless steel containers, *J. Nucl. Mater.*, 478(2016), p. 144.

[2] W. Cao, S. Ge, J.F. Song, C.A. Chen, and D.L. Luo, Deuterium permeation barrier by hot-dipping aluminizing on AISI321 steel, *Int. J. Hydrogen Energy*, 41(2016), No. 48, p. 23125.

[3] K. Udaya Bhat, Mild Steel Plates□: Aluminizing, [in] R. Colás and G. E. Totten Eds. *Encyclopedia of Iron, Steel and Their Alloys* (Five volume set), CRC Press, Boca Raton, 2016, p. 2274.

[4] K. Bouché, F. Barbier, and A. Coulet, Intermetallic compound layer growth between solid iron and molten aluminium, *Mater. Sci. Eng. A*, 249(1998), No. 1-2, p. 167.

[5] D.Q. Wang and Z.Y. Shi, Aluminizing and oxidation treatment of 1Cr18Ni9 stainless steel, *Appl. Surf. Sci.*, 227(2004), No. 1-4, p. 255.

[6] W.J. Cheng and C.J. Wang, Growth of intermetallic layer in the aluminide mild steel during hot-dipping, *Surf. Coat. Technol.*, 204 (2009), No. 6-7, p. 824.

[7] W.J. Cheng and C.J. Wang, Microstructural evolution of intermetallic layer in hot-dipped aluminide mild steel with silicon addition, *Surf. Coat. Technol.*, 205(2011), No. 19, p. 4726.

[8] A. Bouayad, C. Gerometta, A. Belkebir, and A. Ambari, Kinetic interactions between solid iron and molten aluminium, *Mater. Sci. Eng. A*, 363(2003), No. 1-2, p. 53.

[9] S. Kobayashi and T. Yakou, Control of intermetallic compound layers at interface between steel and aluminum by diffusion-treatment, *Mater. Sci. Eng. A*, 338(2002), No. 1-2, p. 44.

[10] V.I. Dybkov, *Solid State Reaction Kinetics*, IPMS Publications, Kiev, 2013, p. 311.

[11] P. Budberg and A. Prince, *Aluminium–Iron–Nickel: Ternary Alloys*, Edited by G. Petzow and G. Effenberg, VCH, Weinheim, 1991, p. 309.

[12] M. Palm, The Al–Cr–Fe system–phases and phase equilibria in the Al-rich corner, *J. Alloys Compd.*, 252(1997), No. 1-2, p. 192.

[13] M.J. Cooper, The structure of the intermetallic phase θ (Cr–Al), *Acta Crystallogr.*, 13(1960), No. 3, p. 257.

[14] T. Ohnishi, Y. Nakatani, and K. Okabayashi, Crystal structures of intermetallic θ, η and ε phases in Al–Cr system, *Bull. Univ. Osaka Prefecture Ser. A*, 24(1976), No. 2, p. 183.

[15] H. Baker and H. Okamoto, ASM Handbook, Vol. 3: *Alloy Phase Diagrams*, ASM International, Materials Park, Ohio, 1992, p. 2.

[16] G. Ghosh, K. Korniyenko, T. Velikanova, and V. Sidorko, *Aluminium–Chromium–Iron (Iron Systems, Part 1)*, Springer, Berlin, 2008, p. 1.

[17] S. Chatterjee T.A. Abinandanan, and K. Chattopadhyay, Phase-field simulation of fusion interface events during solidification of dissimilar welds: effect of composition inhomogeneity, *Metall. Mater. Trans. A*, 39(2008), No. 7, p. 1638.

[18] H.R. Shahverdi, M.R. Ghomashchi, S. Shabestari, and J. Hejazi, Microstructural analysis of interfacial reaction between molten aluminium and solid iron, *J. Mater. Process. Technol.*, 124(2002), No. 3, p. 345.

[19] R.M. Walser and R.W. Bené, First phase nucleation in silicon–transitionmetal planar interfaces, *Appl. Phys. Lett.*, 28 (1976), No. 10, p. 624.

[20] F.M. d'Heurle, Interface reactions with formation of a solid phase on a solid substrate: A short overview, *Mater. Sci. Forum*, 155-156(1994), p. 1.

[21] J. Philibert, Interplay of diffusion and interface processes in multiphase diffusion, *Defect Diffus. Forum*, 95-98(1993), p. 493.

[22] V.N. Yeremenko, Y.V. Natanzon, and V.I. Dybkov, The effect of dissolution on the growth of the Fe_2Al_5, interlayer in the solid iron–liquid aluminium system, *J. Mater. Sci.*, 16(1981), No. 7, p. 1748.

[23] N.J.E. Adkins, N. Saunders, and P. Tsakiropoulos, Rapid solidification of peritectic aluminium alloys, *Mater. Sci. Eng.*, 98(1988), p. 217.

[24] S. Sharafi and M.R. Farhang, Effect of aluminizing on surface microstructure of an HH309 stainless steel, *Surf. Coat. Technol.*, 200(2006), No. 16-17, p. 5048.